

Highly efficient density inversion of gravity data using nonlinear density polynomial fitting

Guoqing Ma¹, Zongrui Li², Lili Li², and Taihan Wang²

ABSTRACT

The density inversion of gravity data is commonly achieved by discretizing the subsurface into prismatic cells and calculating the density of each cell. During this process, a weighting function is introduced to the iterative computation to reduce the skin effect during the inversion. Thus, the computation process requires a significant number of matrix operations, which results in low computational efficiency. We have adopted a density inversion method with nonlinear polynomial fitting (NPF) that uses a polynomial to represent the density variation of prismatic cells in a certain space. The computation of each cell is substituted by the computation of the nonlinear polynomial coefficients. Consequently, the efficiency of the inversion is significantly improved because the number of nonlinear polynomial coefficients is less than the number of cells used.

Moreover, because representing the density change of all of the cells poses a significant challenge when the cell number is large, we adopt the use of a polynomial to represent the density change of a subregion with fewer cells and multiple nonlinear polynomials to represent the density changes of all prism cells. Using theoretical model tests, we determine that the NPF method more efficiently recovers the density distribution of gravity data compared with conventional density inversion methods. In addition, the density variation of a subregion with $8 \times 8 \times 8$ prismatic cells can be accurately and efficiently obtained using our cubic NPF method, which also can be used for noisy data. Finally, the NPF method is applied to real gravity data in an iron mining area in Shandong Province, China. Convergent results of a 3D perspective view and the distribution of the iron ore bodies are acquired using this method, demonstrating the real-life applicability of this method.

INTRODUCTION

It is well known that gravity inversion is often ill-posed and requires certain constraints to guarantee results that are unique and stable (Li and Oldenburg, 1996; Zhdanov and Tartaras, 2002). To reduce nonuniqueness and uncertainty, the subsurface space is usually discretized into cells of constant sizes and density values using 3D density inversion (Blakely, 1995), and a depth weighting function is used to counteract the inherent decay of the kernel function (the “skin effect”) and improve the resolution (Li and Oldenburg, 1996, 1998). However, in real-life applications, significant costs are incurred during large-scale inversion. In recent years, tackling large-scale data inversion has mainly addressed two problems (Davis et al., 2011; Martinez et al., 2013; Farshad et al., 2018):

(1) determining the fast computation method of the forward operator and (2) finding and using an efficient and fast solution process for linear or nonlinear equations. The wavelet compression technique can be used to realize the rapid property inversion of large-scale magnetic data (Portniaguine and Zhdanov, 2002; Li and Oldenburg, 2003). Yao et al. (2003) propose a geometric grid equivalent compression storage technology and the corresponding calculation strategies, which fundamentally improved the calculation speed of nonlinear inversions. According to the local symmetry of the forward kernel matrix in the spatial domain, Jing et al. (2019) use frequency-domain calculations to replace matrix operations in forward and inversion processes to improve computational efficiency.

Manuscript received by the Editor 8 September 2020; revised manuscript received 5 June 2021; published ahead of production 24 August 2021; published online 19 October 2021.

¹Jilin University, College of Geoexploration Science and Technology, Changchun 130026, China; Jilin University, Institute of National Development and Security Studies, Changchun 130012, China; and China State Shipbuilding Corporation, Laboratory of Science and Technology on Marine Navigation and Control, Tianjin 300131, China. E-mail: maguoqing@jlu.edu.cn.

²Jilin University, College of Geoexploration Science and Technology, Changchun 130026, China. E-mail: 2199327023@qq.com; lilili@jlu.edu.cn (corresponding author); wangtaihan@jlu.edu.cn.

© 2021 Society of Exploration Geophysicists. All rights reserved.

Čuma et al. (2012) and Čuma and Zhdanov (2014) convert the inversion to an approximate linear scaling process on a parallel computer, depending on the linear characteristics of the potential field, to improve computational speed. In terms of a fast-solving method, Pilkington (1997) uses a preconditioned conjugate-gradient (PCG) approach to reduce memory requirements and avoid significant matrix multiplications. Wang et al. (2017) propose an improved PCG algorithm, which combines the symmetric successive overrelaxation technique and the incomplete Cholesky decomposition algorithm to achieve rapid inversion of gravity gradiometry data. Pilkington (2008) develops a data-space inversion approach, which uses the Cauchy norm on model parameters to impose the sparseness and enforce the depth weighting. The Lanczos bidiagonalization algorithm appears more efficient and requires less computer RAM, and it was successfully used in potential-field inversion (Rezaie et al., 2016, 2017a, 2017b). Vatankhah et al. (2014) develop a fast algorithm for solving the underdetermined 3D linear gravity inversion problem based on randomized singular-value decomposition. Xu et al. (2020) describe an efficient density inversion approach based on the potential field migration technique.

The subsurface density variation can be represented by a polynomial, whereas the exponential, parabolic, and quadratic polynomial density functions are widely used in interface inversion (Cordell, 1973; Rao, 1986; Santos et al., 2015). Liu et al. (2019) develop the polynomial coefficient inversion method using depth-variable polynomial functions for 2D gravity inversion. García-Abdeslem (2003) demonstrates that the cubic polynomial density function could more efficiently simulate the subsurface density variation to complete the interface inversion. Numerous researchers have conducted research on the forward gravity problem of variable-density bodies. García-Abdeslem (2005) derives an analytic solution of the gravitational anomaly, which was caused by a rectangular prism with a cubic polynomial density variation. Zhou (2009) proposes a semianalytic method to compute the gravitational

anomaly of a rectangular prism, with the density contrast varying in three directions. Ren et al. (2017) use third-order polynomial functions to develop a new singularity-free analytical formula for obtaining the gravity field of arbitrary 3D polyhedral bodies, with horizontally and vertically varying density contrasts. Zhang and Jiang (2017) derive analytical expressions of the gravitational vector field of a 3D rectangular prism with an arbitrary-order polynomial density function.

In this study, we present a density inversion method with nonlinear polynomial fitting (NPF), in which the densities of prismatic cells are represented by a polynomial of the cell positions and the density computation of each cell is substituted by coefficient computations of the polynomial. Moreover, because the number of coefficients is fewer than the number of cells, the calculation efficiency of the NPF method is higher than that of other conventional methods.

DENSITY INVERSION METHOD BASED ON A NONLINEAR POLYNOMIAL

For the density inversion of a gravity anomaly, the subsurface was divided into prismatic cells (the density value of each cell is constant), as shown in Figure 1a, and the density value of each cell was then computed to obtain the density distribution of the subsurface. The density ρ is related to the gravity data by

$$\mathbf{G}\rho = \mathbf{g}_{\text{obs}}, \quad (1)$$

where \mathbf{g}_{obs} is the gravity data and \mathbf{G} is the forward operator. The forward operator \mathbf{G} at the location j ($j = 1, \dots, N$) of the cell k ($k = 1, \dots, M$) is (Haáz, 1953; Li and Oldenburg, 1998)

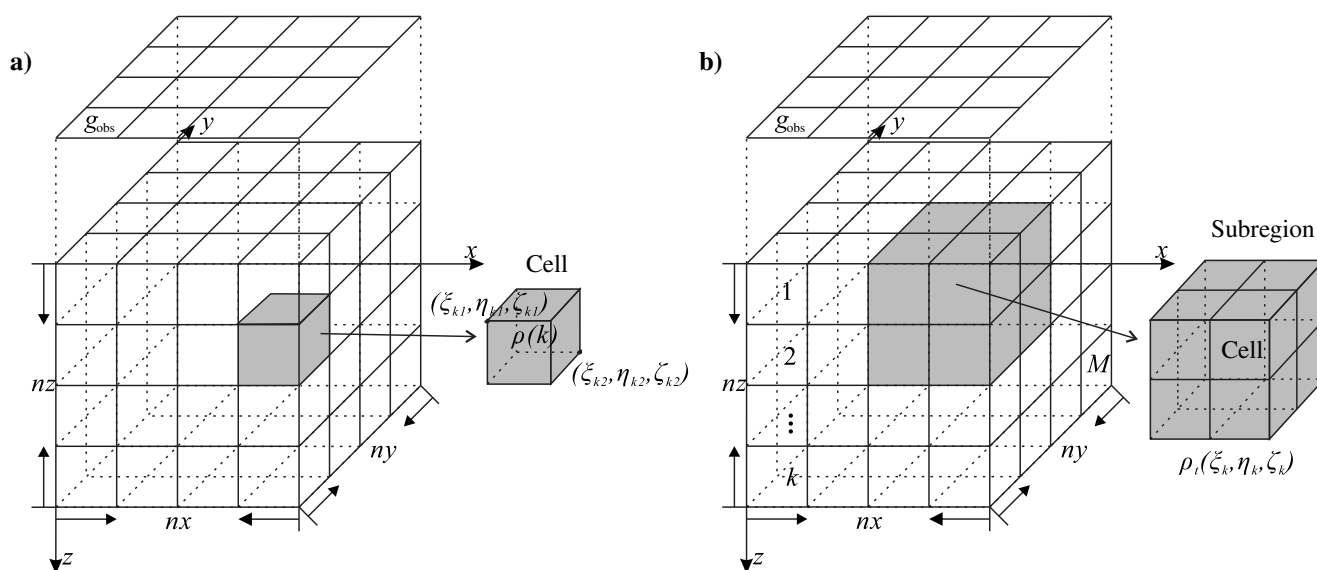


Figure 1. (a) Discretization of the subsurface by prism cells and (b) representation of the density distribution of the subregion with several prism cells using a polynomial.

$$G(j, k) = \sum_{w=1}^2 \sum_{v=1}^2 \sum_{u=1}^2 \gamma \left\{ -(x_j - \xi_{k,u}) \ln[r + (y_j - \eta_{k,v})] - (y_j - \eta_{k,v}) \ln[r + (x_j - \xi_{k,u})] + (z_j - \zeta_{k,w}) \arctan \frac{(x_j - \xi_{k,u})(y_j - \eta_{k,v})}{(z_j - \zeta_{k,w})r} \right\}, \quad (2)$$

where $\gamma = 6.672 \times 10^{-11} \text{ m}^3/(\text{kg} \cdot \text{s}^2)$ is the universal gravitational constant; $(\xi_{k,1}, \eta_{k,1}, \zeta_{k,1})$ and $(\xi_{k,2}, \eta_{k,2}, \zeta_{k,2})$ represent the minimum and maximum coordinates of the cell k , respectively; $r = \sqrt{(x_j - \xi_{k,u})^2 + (y_j - \eta_{k,v})^2 + (z_j - \zeta_{k,w})^2}$, (x_j, y_j, z_j) is the coordinate of the observation point; N is the total number of prismatic cells; and M is the total number of observation points.

The minimum norm inversion method (Tikhonov and Arsenin, 1977) is commonly used to obtain the density distribution, in which the objective function is described by

$$\phi(\rho) = \lambda \phi_m(\rho) + \phi_d(\rho) = \lambda \|\mathbf{W}_\rho(\rho - \rho_0)\|_2^2 + \|\mathbf{W}_d(\mathbf{G}\rho - \mathbf{g}_{\text{obs}})\|_2^2, \quad (3)$$

where $\phi(\rho)$ is the data misfit, \mathbf{W}_d is the standard deviation error, $\phi_m(\rho)$ is the objective function of density, ρ_0 is the reference model density vector, ρ is the cell density vector, and λ is a Lagrange multiplier. Equation 3 is an objective function of the minimum norm method. Because of the skin effect, the sensitivity (\mathbf{G} values) of the gravity data decays with depth, and the inversion results are typically close to the near-surface results. Therefore, $\mathbf{W}_\rho = (z + z_0)^{-\beta/2}$, a common weighting matrix, can be used to counteract this inherent decay (Li and Oldenburg, 1996, 1998).

This study presents a high-efficiency density inversion method that uses a nonlinear polynomial to represent the density variations of prism cells and computes the polynomial coefficients to replace the density calculation of each cell; this improves the computation efficiency of the proposed method because the number of coefficients is less than the number of cells. The NPF method still obtains the density of each cell; however, the efficiency of this method is improved by changing the computation technique, and the memory of this method is the same as that of conventional methods.

The density of each cell in the NPF method is constant and equal to the polynomial related to its center point position. It is difficult to use a polynomial to simulate the density variations of the whole region when the number of cells is large; therefore, in this method, we divided the whole region into several subregions, and each subregion uses a 3D polynomial to fit the density variation. As shown in Figure 1b, the subsurface was evenly divided into multiple subregions, each of which contains multiple prism cells. The density variation in each subregion conforms to the same polynomial, and the equation for obtaining the density of the cell in the subregion t ($t = 1, \dots, N_{\text{sub}}$) is as follows (García-Abdeslem, 2005; Zhou, 2009; D'Urso and Trotta, 2017; Ren et al., 2017):

$$\begin{aligned} \rho_t(\xi, \eta, \zeta) &= c_{t(0,0,0)} \xi^0 \eta^0 \zeta^0 + \dots + c_{t(l,0,0)} \xi^l \eta^0 \zeta^0 + \dots \\ &+ c_{t(0,m,0)} \xi^0 \eta^m \zeta^0 + \dots + c_{t(0,0,n)} \xi^0 \eta^0 \zeta^n + \dots + c_{t(l,m,n)} \xi^l \eta^m \zeta^n \\ &= \sum_{l=0}^{s_t} \sum_{m=0}^{s_t-l} \sum_{n=0}^{s_t-l-m} c_{t(l,m,n)} \xi^l \eta^m \zeta^n, \end{aligned} \quad (4)$$

where s_t is the highest degree of the polynomial, c_t is the coefficient of the polynomial, N_{sub} is the number of subregions, and (ξ, η, ζ) is the center point of the cell.

Then, the gravity field \mathbf{g}_{obs} can be computed using

$$\mathbf{g}_{\text{obs}} = \mathbf{V} \cdot \mathbf{c}, \quad (5)$$

where $\mathbf{c} = [\mathbf{c}_1 \ \mathbf{c}_t \ \dots \ \mathbf{c}_{N_{\text{sub}}}]$, $\mathbf{c}_t = [\mathbf{c}_{t(0,0,0)} \ \dots \ \mathbf{c}_{t(l,m,n)}]$, \mathbf{V} is the kernel function for the NPF method, and

$$V_{i,(l,m,n)} = \gamma \sum_{t=1}^{N_{\text{sub}}} \xi_t^l \eta_t^m \zeta_t^n \oint_{v_i} \frac{(z_i - \zeta)}{[(x_j - \xi_{k,u})^2 + (y_j - \eta_{k,v})^2 + (z_j - \zeta_{k,w})^2]^{3/2}} dv. \quad (6)$$

Thus, the objective function of the density inversion using a polynomial can be given as

$$\phi(\mathbf{c}) = \|\mathbf{V}\mathbf{c} - \mathbf{g}_{\text{obs}}\|_2^2. \quad (7)$$

Moreover, the optimal solution of \mathbf{c} can be obtained by solving the minimum value of $\phi(\mathbf{c})$. Similarly, using the minimum norm inversion method (Tikhonov and Arsenin, 1977), the following objective function can be obtained to solve equation 5:

$$\phi(\mathbf{C}) = \lambda_c \phi_c(\mathbf{C}) + \phi_d(\mathbf{C}) = \lambda_c \|\mathbf{W}_c(\mathbf{C} - \mathbf{C}_0)\|_2^2 + \|\mathbf{V}\mathbf{C} - \mathbf{g}_{\text{obs}}\|_2^2, \quad (8)$$

where λ_c is a Lagrange multiplier, $\mathbf{W}_c = \mathbf{W}_\rho \cdot \mathbf{P}$, $\mathbf{P} = \text{diag}([\mathbf{P}_1 \ \mathbf{P}_t \ \dots \ \mathbf{P}_{N_{\text{sub}}}]^T)$, $\mathbf{P}_t = [\mathbf{P}_{t,1}^T \ \mathbf{P}_{t,k}^T \ \dots \ \mathbf{P}_{t,N_{\text{sub},k}}^T]^T$, N_t is the number of cells in the t th subregion, $\mathbf{P}_{t,k} = [\xi_k^0 \eta_k^0 \zeta_k^0 \ \dots \ \xi_k^m \eta_k^n \zeta_k^l]$, and (ξ_k, η_k, ζ_k) is the center point of the k th cell of the subsurface.

For solving equation 8, a linear system of equations has to be solved. The conjugate-gradient algorithm method can solve this system with reduced memory requirements by avoiding large matrix multiplications (Pilkington, 1997; Zhdanov and Tartaras, 2002). In the computation, we used the conjugate-gradient method to iteratively calculate the minimum value of $\phi(\mathbf{c})$ and the misfit error was computed using $\sqrt{\|\mathbf{g}_{\text{obs}} - \mathbf{V} \cdot \mathbf{c}\|_2^2 / M}$.

Overall, the following calculation process was used to solve the linear system of equations:

- 1) Calculate matrix \mathbf{V} .
- 2) Calculate matrix \mathbf{W}_c .
- 3) Set the initial value of the array \mathbf{c} (\mathbf{c}_0 can be given by the initial fitting of the prior density model. In our test, the a priori model was not used; therefore, \mathbf{C}_0 is a vector of zero).
- 4) Use the conjugate-gradient method (Pilkington, 1997) to calculate \mathbf{C} , and the misfit error of this calculation result is calculated for each iteration. In this study, the loop ended when the misfit error was less than 0.01 mGal.
- 5) Finally, use equation 4 to obtain the density of any subsurface cell.

THEORETICAL MODEL TESTS

Synthetic gravity anomalies were used to test the application of the NPF method, and all of the gravity anomalies used in this study consisted of 32×32 data. Figure 2a shows the gravity anomaly using a standard cubic model with a size of $2 \times 2 \times 2$ km, density of 800 kg/m^3 , and center at (5, 5, 2) km. In the inversions, the subsurface was discretized into prismatic cells, with the horizontal interval of each cell being equal to the sampling interval; this was based on the findings of previous studies, which revealed that the density inversion method can obtain more reasonable results when the horizontal size of the prism is close to the sampling interval (Li and Oldenburg, 1996; Boulanger and Chouteau, 2001). The subsurface was divided into $32 \times 32 \times 32$ prism cells. The

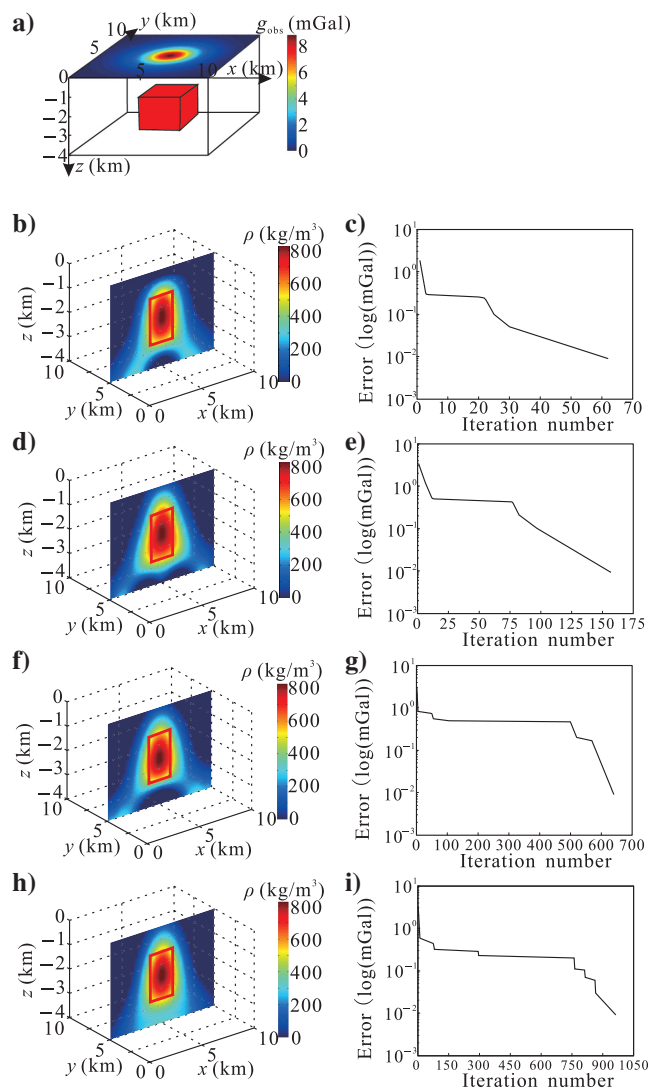


Figure 2. (a) A $2 \times 2 \times 2$ km cubic model and the gravity anomaly, (b) vertical slice at $y = 5.0$ km inverted by the quadratic NPF method, (c) data misfit error of the result in (b), (d) vertical slice at $y = 5.0$ km inverted by the cubic NPF method, (e) data misfit error of the result in (d), (f) vertical slice with $y = 5.0$ km inverted by the quartic NPF method, (g) data misfit error of the result in (e), (h) vertical slice at $y = 5.0$ km inverted by the quadratic NPF method, and (i) data misfit error of the result in (h).

iteration termination condition of the inversion was that the misfit error does not exceed 0.01 mGal up to 1000 iterations. Figure 2b and 2c indicates that the density inversion result and misfit error varied with the number of iterations computed by the NPF method, using a second-degree 3D polynomial with 10 coefficients. The red box represents the true range of the model. The high-density distribution at the bottom of the inversion result does not correspond to the actual position of the model. Figure 2d and 2e shows the density inversion result and misfit error computed by the NPF method with a third-degree 3D polynomial using 20 coefficients. This inversion result was more similar to the actual range than the result obtained with the second-degree polynomial because the density distribution of the inversion results is consistent with the actual position of the model. Figure 2f and 2g shows the density inversion result and misfit error computed by the NPF method with a fourth-degree 3D polynomial using 35 coefficients. In this case, the inversion result is further improved; however, the result still deviates from the true range. Figure 2h and 2i shows the density inversion result and misfit error computed by the NPF method with a fifth-degree 3D polynomial using 56 coefficients. In this case, accurate inversion results were obtained; however, this computation required 951 iterations to obtain a result. Therefore, it is difficult to obtain correct results using a nonlinear polynomial when the number of prism cells is large and the computation efficiency is low.

To obtain more reasonable results, we divided the model domain into several subregions with fewer cells and used a polynomial to represent the density variation of each subregion. The density variation of all cells was characterized by multiple polynomials. The model domain was divided into $4 \times 4 \times 4$ subregions, and each subregion contained $8 \times 8 \times 8$ prismatic cells. The effects of different degrees of NPFs on the subregion inversion method and misfit error computed by the subregion NPF method with a second-degree 3D polynomial using $4 \times 4 \times 4 \times 10$ coefficients, and the actual location has been labeled by the red box line. The density inversion result is close to the real location of the prism; however, several differences exist between the bottom of the inversion results and the actual position of the model. Figure 3c and 3d represents the density inversion result and misfit error computed by the NPF method with a third-degree 3D polynomial using $4 \times 4 \times 4 \times 20$ coefficients. The inversion result is consistent with the actual position of the model and can correctly describe the source distribution. Figure 3e and 3f represents the density inversion result and misfit error computed by the NPF method with a fourth-degree 3D polynomial using $4 \times 4 \times 4 \times 35$ coefficients. The inversion result is more convergent and accurate, but the number of iterations tends to increase. Therefore, the cubic NPF method is sufficient to compute the density variation of a subregion with $8 \times 8 \times 8$ cells.

In addition, we used the gravity anomaly shown in Figure 2a to test the difference between the results of the NPF method and the minimum norm method. In the conventional inversion process, the subsurface is discretized into $32 \times 32 \times 32$ prism cells; however, in our method, the entire underground is divided into $4 \times 4 \times 4$ subregions, each subregion contains $8 \times 8 \times 8$ prism units, and the density distribution of each subregion is represented by a third-degree 3D polynomial using $4 \times 4 \times 4 \times 20$ coefficients. Figure 4a and 4b represents the horizontal slices of the density inversion results at a depth of -2.0 km, which are computed using the proposed method

and the minimum norm method, respectively. Figure 4c and 4d indicates the vertical slices of the density inversion results at the y -coordinate value of 5.0 km, which have been computed using the proposed method and the minimum norm method, respectively. The true position of the prism model is indicated by the red rectangle. The inversion results of both methods are similar to the real distribution of the cube model. It can be seen that the inversion model using the proposed NPF method is more compact and exhibits finer spatial contrasts. Figure 4e and 4f presents the 3D perspective view of the density-contrast model having a density greater than 400 kg/m^3 for the two methods, which illustrates the finer spatial contrasts.

To test the inversion effect of the presented method on noisy data, we added Gaussian noise with a signal-to-noise ratio (S/N) of 15 to the data n order to test the inversion effect of the presented method on noisy data, and we added Gaussian noise with an S/N of 15 to the data shown in Figure 2a, as is shown in Figure 5a. We divided the region into $4 \times 4 \times 4$ subregions in a manner similar to that shown in Figure 1b, and each subregion contains $8 \times 8 \times 8$ cells. A third-degree 3D polynomial was then applied to each subregion. Figure 5b shows the horizontal slices of the density inversion results at a depth of -2.0 km , and Figure 5c represents the vertical slices of the density inversion results at the y -coordinate of 5.0 km. Meanwhile, Figure 5d shows a 3D perspective view. Using the proposed NPF method for the inversion of noisy data, we obtained a convergent result. Comparing these inversion results to those shown in Figure 4a, 4c, and 4e revealed a maximum differential value of 0.1 kg/m^3 between them. Hence, using this method produced stable results when calculating the inversion result for a noisy anomaly.

The efficiencies of the nonlinear polynomial inversion method and the minimum structure inversion method were compared using different subdivision numbers in the same area. The complete calculation time for both methods was determined under the same subdivision numbers in the same area. Both of the inversion calculations were performed on the same computer with a CPU frequency of 1.70 GHz and memory of 16 GB. MATLAB R2014a software was used for programming and calculation purposes, and serial algorithms were applied in the programming process. Figure 6 shows the calculation time of the different number of cells. The results indicate that the time cost of the NPF inversion method was similar to that of the traditional method when the number of cells is small. However, with an increasing number of cells, the efficiency of the nonlinear polynomial density inversion method is significantly higher than the minimum norm method. Therefore, this method is more suitable for large-scale data inversions.

Next, we used the two-prism model to determine the efficiency of the NPF method. Figure 7a shows the synthetic gravity anomaly of the two-prism

model. Both of the prisms are cubical with density of 800 kg/m^3 and a side length of 2 km. The center coordinates are (3, 5, 2) km and (7, 5, 2) km, respectively. Figure 7b shows the horizontal slice of the inversion result at $z = -2.0 \text{ km}$ and reveals that the calculated location is consistent with the real source. Figure 7c indicates the vertical slice of the inversion result at $y = 5.0 \text{ km}$, and Figure 7d provides the 3D perspective view. Overall, we determined that the location and boundary information of the inversion results correspond well with the real model.

To verify the feasibility of using the NPF method for processing data with a discontinuous and continuous density distribution, we used three adjacent prismatic bodies to represent the discontinuous density distribution. Figure 8a shows the model and synthetic gravity anomaly. This model consists of three adjacent prisms of the same size and density, with center coordinates of (3, 5, 1.5) km, (5, 5, 2) km, and (7, 5, 2.5) km. The side lengths in the x -, y -, and z -directions are 2, 2, and 1 km, respectively, and the density of the prisms is 800 kg/m^3 . Figure 8c shows the results of the NPF method, which illustrates that the inversion results can reflect the density structure characteristics. Figure 8b indicates that

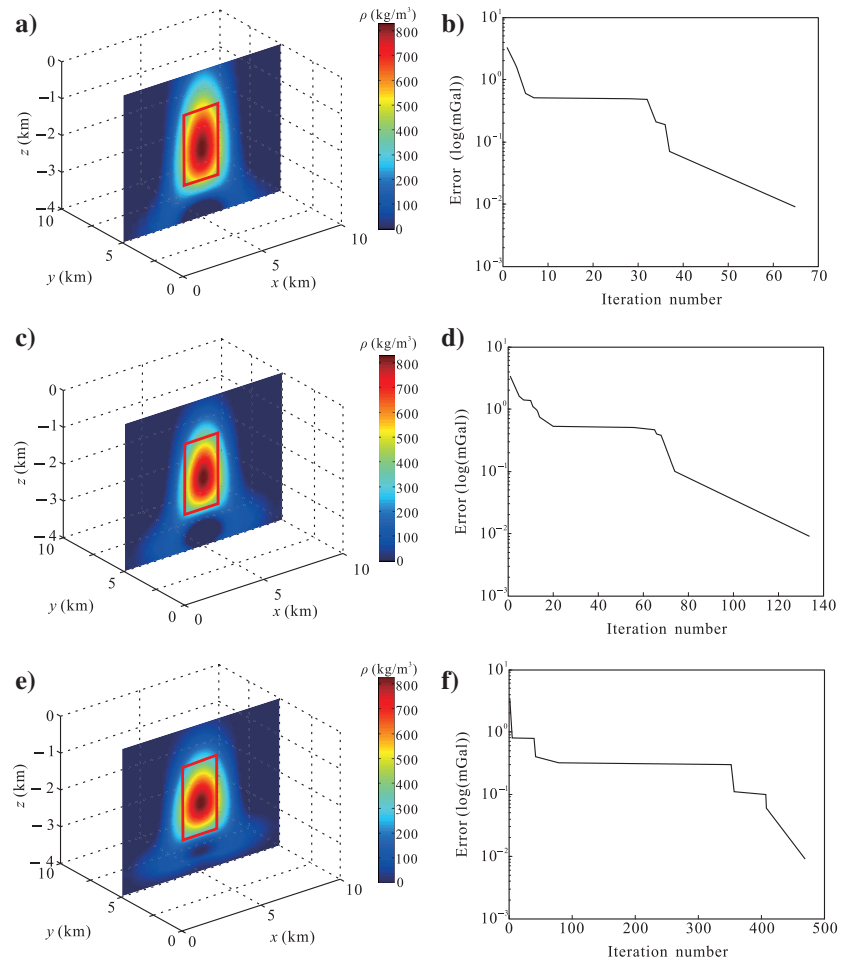


Figure 3. (a) Vertical slice at $y = 5.0 \text{ km}$ inverted by the quadratic NPF method with the subregion fitting approach, (b) data misfit error of the result in (a), (c) vertical slice at $y = 5.0 \text{ km}$ inverted by the cubic NPF method with the subregion fitting approach, (d) misfit error curve of the calculation result in (c), (e) vertical slice at $y = 5.0 \text{ km}$ inverted by the quartic NPF method with the subregion fitting approach, and (f) data misfit error of the result in (e).

Figure 4. (a) Horizontal slice at $z = -2.0$ km using the NPF method, (b) horizontal slice at $z = -2.0$ km using the minimum norm inversion method, (c) vertical slice at $y = 5.0$ km using the NPF method, (d) vertical slice at $y = 5.0$ km using the minimum norm inversion method, (e) 3D perspective view with density greater than 400 kg/m^3 using the NPF method, and (f) 3D perspective view with density greater than 400 kg/m^3 using the minimum norm inversion method.

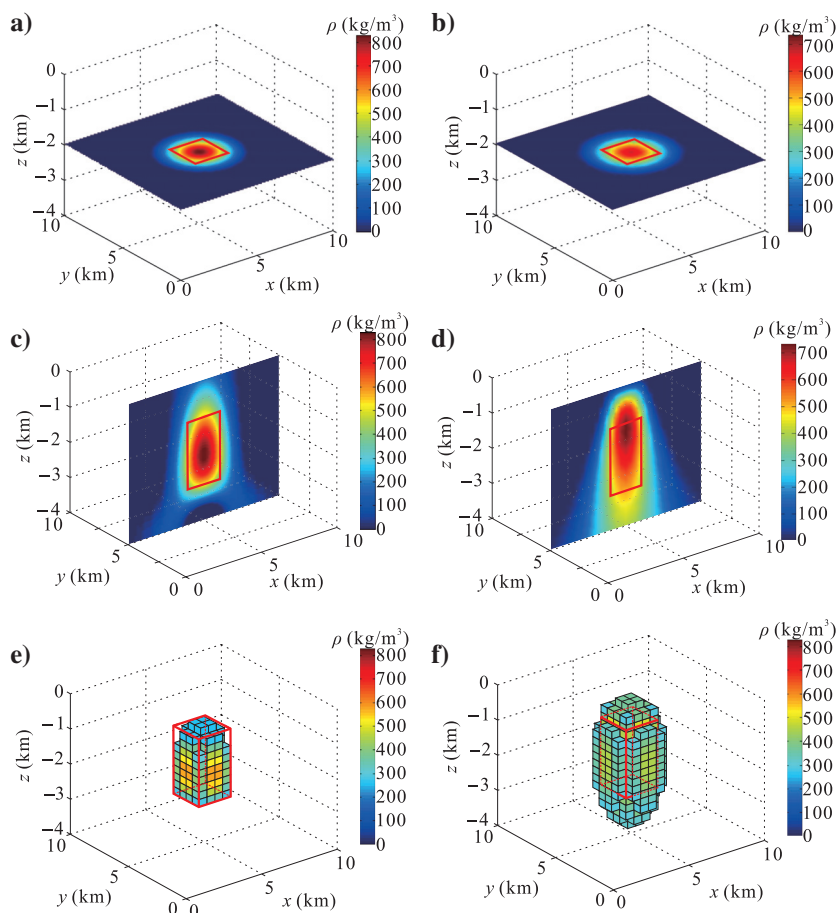
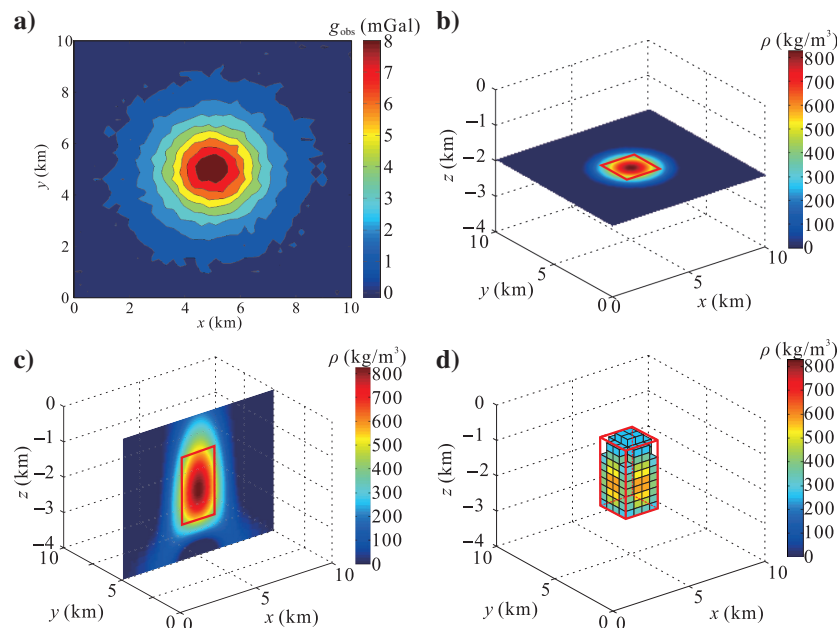


Figure 5. (a) Noise-corrupted gravity anomaly, (b) horizontal slice at $z = -2.0$ km using the NPF method, (c) vertical slice at $y = 5.0$ km using the NPF method, and (d) 3D perspective view with density exceeding 400 kg/m^3 using the NPF method.



the model slices of the continuous density distribution, synthetic gravity anomaly, and model density distribution can be represented by the following equation:

$$\rho(x, y, z) = 1200 - \sqrt{6} \times \sqrt{(x-5000)^2 + (y-5000)^2 + (z-2000)^2} / 15 (\text{kg/m}^3). \quad (9)$$

Figure 8d displays the inversion results of the continuous density model, which reflects the subsurface density distribution. The center position of the inversion result is consistent with the model, and the density distribution is similar to the real model. Figure 8e and 8f shows the comparison of the predicted vertical density distribution and the actual density at two points below the model that are shown in Figure 8c and 8d, respectively; the size and variation trend of the inversion results resemble the model parameters.

REAL-LIFE APPLICATION

Our study area is located in Qihe City, northwestern Shandong Province, China, where numerous magnetic skarn iron deposits are distributed. According to previous geologic studies of the area, limestone of the Ordovician Majiagou Formation serves as the ore-controlling host rock, and it includes gabbro, diorite, and diorite porphyry. The ore bodies typically occur in the contact zone between the rock mass and the surrounding rock (Zhang et al., 2019). Skarnization is an alteration phenomenon that occurs in rocks and is closely related to mineralization. In the study area, skarn deposits are primarily situated at the top and bottom of the ore bodies; they typically manifest as magnetite deposits formed due to high-temperature hydrothermal contact metasomatism caused by intermediate-base intrusive rocks. Moreover, skarn deposits are distributed in the upper parts of the high-density intrusive rocks. The iron ore in the region has mostly developed on the periphery of faults, and the approximate distribution of these minerals can be deduced from geologic data and regional fault distributions, which are shown in Figure 9a.

To establish the specific distribution of mineral resources in the region, a high-precision airborne gravity survey was conducted with an average flight height of 86 m and line spacing of 200 m. The lines were also leveled and filtered to attenuate noise. Following the methods presented by Guspí (1987) and Pilkington and Urquhar (1990), we converted the observed data into a horizontal plane with an average altitude of 86 m (Figure 9b). According to the distribution of mineral resources in the upper part of the high-density intrusive rock, three favorable mineral resources were initially determined based on the characteristics of the strong amplitude anomalies. Ore bodies in the study area are typically distributed in a north-south direction and are developed along faults.

We evenly divided the 0–1.2 km subsurface into $3 \times 5 \times 2$ subregions. Each subregion contained $8 \times 8 \times 8$ prismatic cells of the same size.

Therefore, the area was divided into $24 \times 40 \times 16$ cells. In the NPF method, the conjugate-gradient method was used to solve the matrix and the iteration stopped when the misfit error was less than 0.01 mGal. Figure 10a shows the density logging results and density curve obtained by using the NPF method. It is evident that the two curves show the same trend, indicating that the NPF method can be practically applied to reflect the density distribution of an area. Figure 10b shows the 3D density results with a density threshold obtained from the logging data, as shown in Figure 10a. The gravity anomaly of the mineral deposits is plotted above the model, and the location of the borehole is marked. Figure 11 shows the

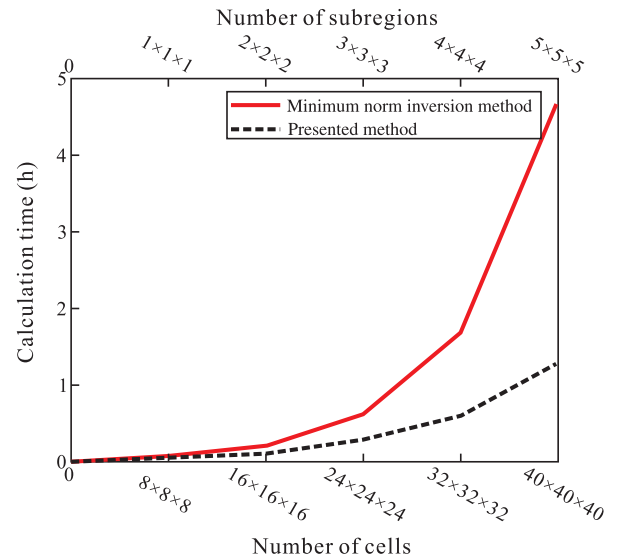


Figure 6. Comparison of the calculation efficiency of the minimum norm inversion and NPF methods.

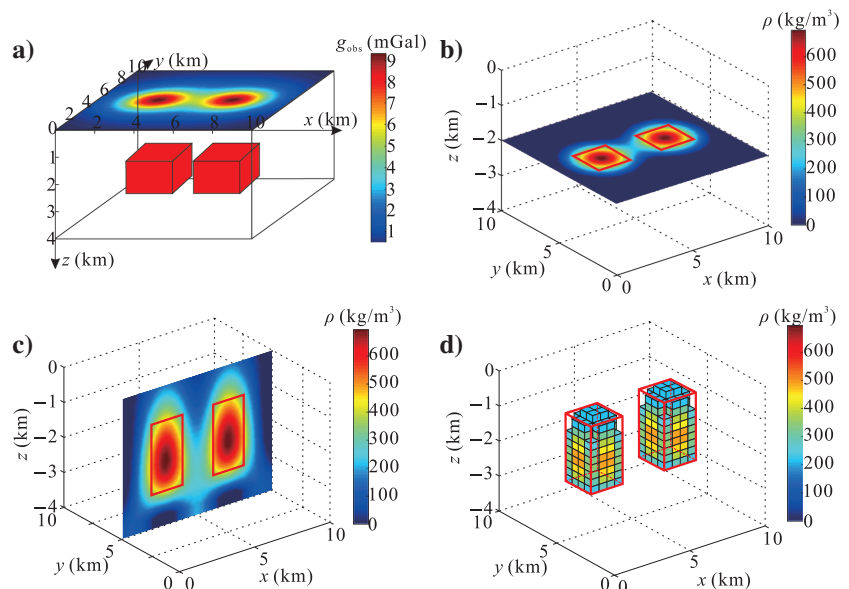


Figure 7. (a) Two cuboid models and synthetic gravity anomaly, (b) horizontal slice at $z = -2.0$ km using the NPF method, (c) vertical slice at $y = 5.0$ km using the NPF method, and (d) 3D perspective view with density greater than 400 kg/m^3 using the NPF method.

Figure 8. (a) Step model with three cuboids and the synthetic gravity anomaly, (b) continuous density change model and its synthetic gravity anomaly, (c) vertical slice at $y = 5.0$ km for the step model data, (d) slices at $x = 5.0$ km, $y = 5.0$ km, and $z = -2.0$ km of the continuous density model data, (e) comparison of the predicted vertical density distribution and the true density below the location of the model in (c), and (f) comparison of the predicted vertical density distribution and true density below the location of the model in (d).

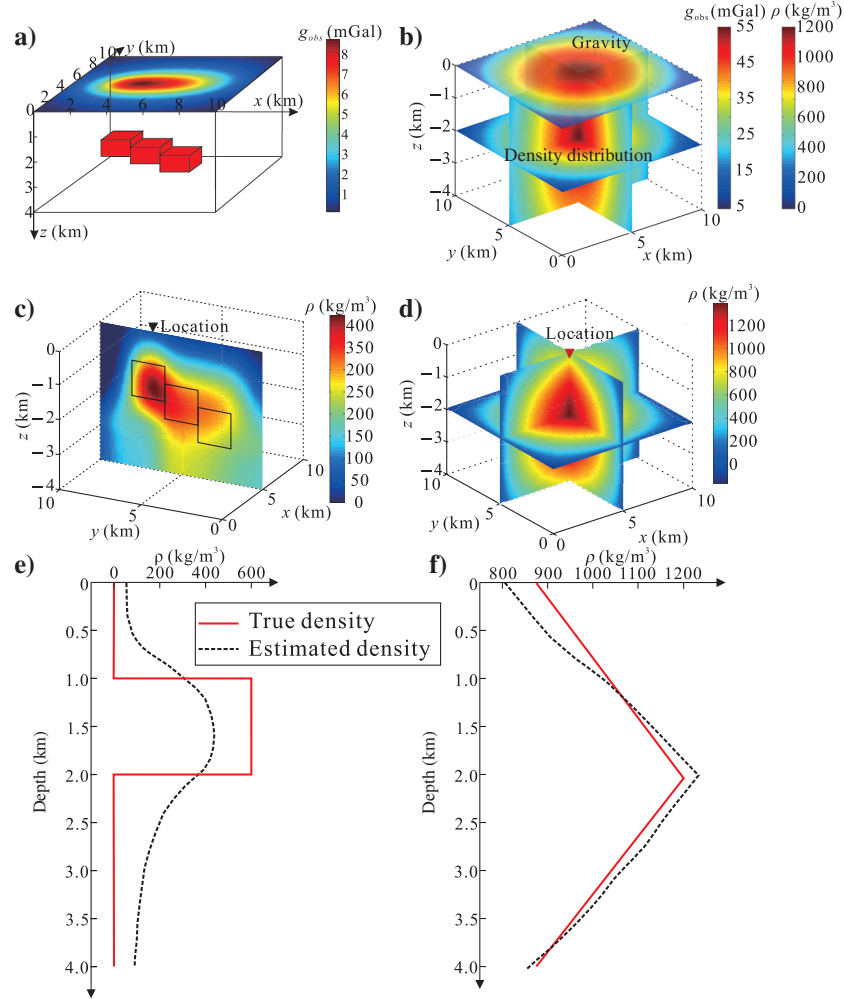
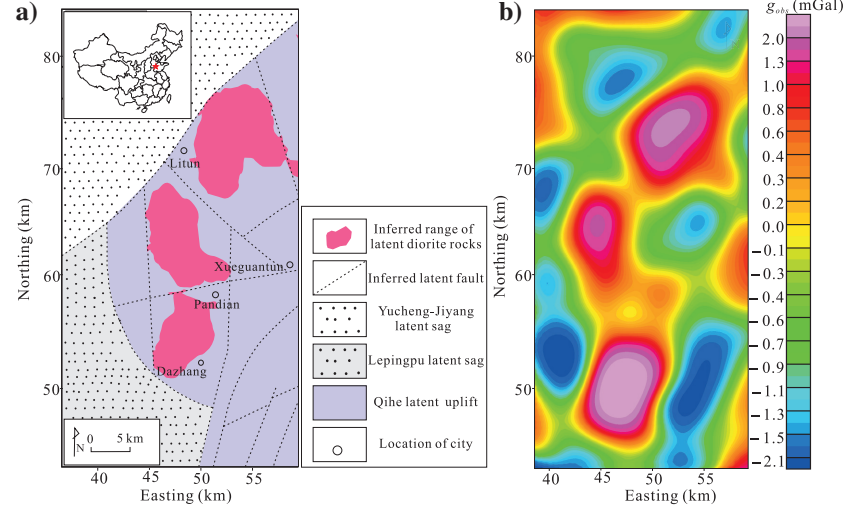


Figure 9. (a) Geologic map of the survey area and (b) residual gravity anomaly of the survey area.



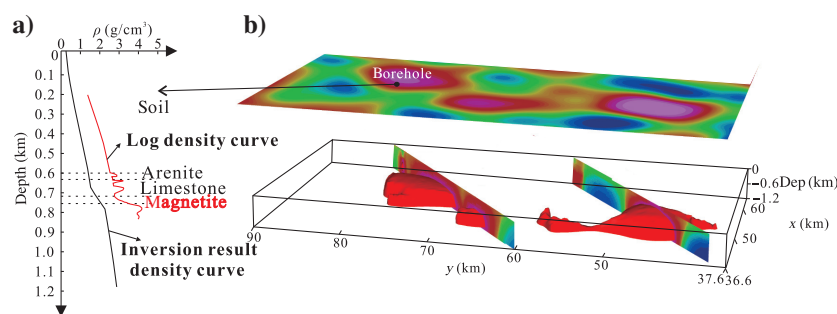


Figure 10. (a) Density logging data curve and recovered density curve and (b) 3D perspective view of the results with densities exceeding 0.4 g/cm^3 .

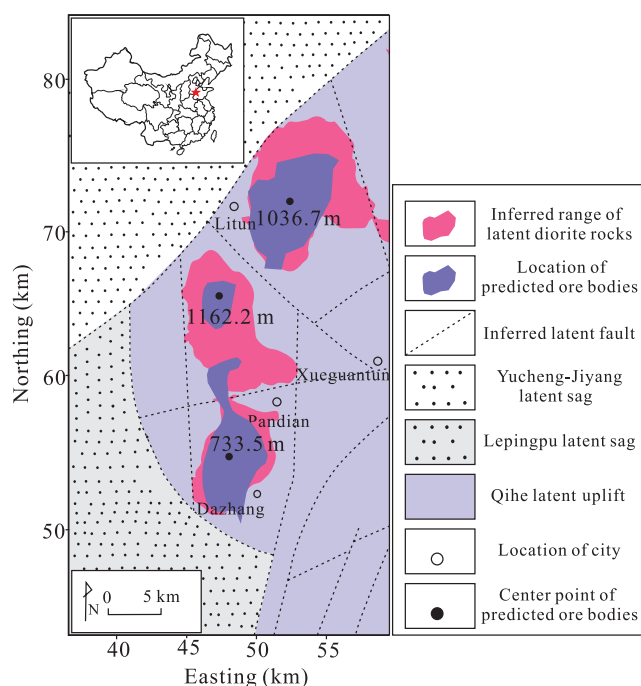


Figure 11. Revised distribution of the mineral resources.

interpreted ore body distributions, locations, and depths associated with the center points of the ore bodies in the study area. The interpretation results in Figure 11 provide essential baseline information for the next stages of resource exploration in the study area.

CONCLUSION

In this study, we have proposed a high-efficiency density inversion method with NPF to accurately calculate the density of subsurface bodies by discretizing them into prismatic cells. The NPF method uses the computed coefficients of nonlinear polynomials to substitute the density computation of each cell. The computation efficiency of the proposed method is improved because the number of coefficients of the nonlinear polynomial is fewer than the number of cells. Synthetic model tests showed that the NPF method can accurately and efficiently be used to calculate density characteristics; they also can be applied to interpret noisy data. To test the real-life application of the method, the method was applied to determine the distribution of

iron ore bodies in the Shandong Province, China. The produced results are consistent with the density log curve, which verified the effectiveness and practicability of the proposed NPF method.

ACKNOWLEDGMENTS

This research was funded by the National Natural Science Foundation of China (42074147), the National Key Research and Development Program Issue During the 13th Five-year Plan Period (2017YFC0602203), the Excellent Young Talents Fund Project of Jilin Province (20190103011JH), the Ministry of Education, and the China Postdoctoral Science Foundation (2019M651209), Laboratory of Science and Technology on Marine Navigation and Control, and China State Shipbuilding Corporation. The authors thank the four anonymous reviewers and B. Cartwright, as well as the editors, for their constructive comments and suggestions.

DATA AND MATERIALS AVAILABILITY

Data associated with this research are confidential and cannot be released.

REFERENCES

- Blakely, R. J., 1995, Potential theory in gravity and magnetic applications: Cambridge University Press.
- Boulanger, O., and M. Chouteau, 2001, Constraints in 3D gravity inversion: *Geophysical Prospecting*, **49**, 265–280, doi: [10.1046/j.1365-2478.2001.00254.x](https://doi.org/10.1046/j.1365-2478.2001.00254.x).
- Cordell, L., 1973, Gravity analysis using an exponential density-depth function — San Jacinto Graben, California: *Geophysics*, **38**, 684–690, doi: [10.1190/1.1440367](https://doi.org/10.1190/1.1440367).
- Čuma, M., G. A. Wilson, and M. S. Zhdanov, 2012, Large-scale 3D inversion of potential field data: *Geophysical Prospecting*, **60**, 1186–1199, doi: [10.1111/j.1365-2478.2011.01052.x](https://doi.org/10.1111/j.1365-2478.2011.01052.x).
- Čuma, M., and M. S. Zhdanov, 2014, Massively parallel regularized 3D inversion of potential fields on CPUs and GPUs: *Computers and Geosciences*, **62**, 82–87, doi: [10.1016/j.cageo.2013.10.004](https://doi.org/10.1016/j.cageo.2013.10.004).
- Davis, K., M. A. Kass, and Y. Li, 2011, Rapid gravity and gravity gradiometry terrain corrections via an adaptive quadtree mesh discretization: *Exploration Geophysics*, **42**, 88–97, doi: [10.1071/EG10016](https://doi.org/10.1071/EG10016).
- D'Urso, M. G., and S. Trotta, 2017, Gravity anomaly of polyhedral bodies having a polynomial density contrast: *Surveys in Geophysics*, **38**, 781–832, doi: [10.1007/s10712-017-9411-9](https://doi.org/10.1007/s10712-017-9411-9).
- Farshad, J., M. Ali, and D. A. Faramarz, 2018, An improved 3D joint inversion method of potential field data using cross-gradient constraint and LSQR method: *Pure and Applied Geophysics*, **175**, 4389–4409, doi: [10.1007/s00024-018-1909-7](https://doi.org/10.1007/s00024-018-1909-7).
- García-Abdeslem, J., 2003, 2D modeling and inversion of gravity data using density contrast varying with depth and source-basement geometry described by the Fourier series: *Geophysics*, **68**, 1909–1916, doi: [10.1190/1.1635044](https://doi.org/10.1190/1.1635044).
- García-Abdeslem, J., 2005, The gravitational attraction of a right rectangular prism with density varying with depth following a cubic polynomial: *Geophysics*, **70**, no. 6, J39–J42, doi: [10.1190/1.2122413](https://doi.org/10.1190/1.2122413).
- Guspi, F., 1987, Frequency-domain reduction of potential field measurements to a horizontal plane: *Geosurveying*, **24**, 87–98, doi: [10.1016/0016-7142\(87\)90083-4](https://doi.org/10.1016/0016-7142(87)90083-4).
- Haáz, I. B., 1953, Relations between the potential of the attraction of the mass contained in a finite rectangular prism and its first and second derivatives: *Geofizikai Közlemények*, **2**, 57–66.
- Jing, L., C. Yao, Y. Yang, M. Xu, G. Zhang, and R. Ji, 2019, Optimization algorithm for rapid 3D gravity inversion: *Applied Geophysics*, **16**, 507–518, doi: [10.1007/s11770-019-0781-2](https://doi.org/10.1007/s11770-019-0781-2).
- Li, Y., and D. W. Oldenburg, 1996, 3-D inversion of magnetic data: *Geophysics*, **61**, 394–408, doi: [10.1190/1.1443968](https://doi.org/10.1190/1.1443968).
- Li, Y., and D. W. Oldenburg, 1998, 3-D inversion of gravity data: *Geophysics*, **63**, 109–119, doi: [10.1190/1.1444302](https://doi.org/10.1190/1.1444302).

- Li, Y., and D. W. Oldenburg, 2003, Fast inversion of large-scale magnetic data using wavelet transforms and a logarithmic barrier method: *Geophysical Journal International*, **152**, 251–265, doi: [10.1046/j.1365-246X.2003.01766.x](https://doi.org/10.1046/j.1365-246X.2003.01766.x).
- Liu, J., J. Zhang, L. Jiang, Q. Lin, and L. Wan, 2019, Polynomial-based density inversion of gravity anomalies for concealed iron-deposit exploration in North China: *Geophysics*, **84**, no. 5, B325–B334, doi: [10.1190/geo2018-0740.1](https://doi.org/10.1190/geo2018-0740.1).
- Martinez, C., Y. Li, R. Krahenbuhl, and M. A. Braga, 2013, Case history 3D inversion of airborne gravity gradiometry data in mineral exploration: A case study in the Quadrilátero Ferrífero, Brazil: *Geophysics*, **78**, no. 1, B1–B11, doi: [10.1190/geo2012-0106.1](https://doi.org/10.1190/geo2012-0106.1).
- Pilkington, M., 1997, 3-D magnetic imaging using conjugate gradients: *Geophysics*, **62**, 1132–1142, doi: [10.1190/1.1444214](https://doi.org/10.1190/1.1444214).
- Pilkington, M., 2008, 3D magnetic data-space inversion with sparseness constraints: *Geophysics*, **74**, no. 1, L7–L15, doi: [10.1190/1.3026538](https://doi.org/10.1190/1.3026538).
- Pilkington, M., and W. E. S. Urquhart, 1990, Reduction of potential field data to a horizontal plane: *Geophysics*, **55**, 549–555, doi: [10.1190/1.1442866](https://doi.org/10.1190/1.1442866).
- Portniaguine, O., and M. S. Zhdanov, 2002, 3-D magnetic inversion with data compression and image focusing: *Geophysics*, **67**, 1532–1541, doi: [10.1190/1.1512749](https://doi.org/10.1190/1.1512749).
- Rao, D. B., 1986, Modelling of sedimentary basins from gravity anomalies with variable density contrast: *Geophysical Journal Royal Astronomical Society*, **84**, 207–212, doi: [10.1111/j.1365-246X.1986.tb04353.x](https://doi.org/10.1111/j.1365-246X.1986.tb04353.x).
- Ren, Z., Y. Zhong, C. Chen, J. Tang, and K. Pan, 2017, Gravity anomalies of arbitrary 3D polyhedral bodies with horizontal and vertical mass contrasts up to cubic order: *Geophysics*, **83**, no. 1, G1–G13, doi: [10.1190/geo2017-0219.1](https://doi.org/10.1190/geo2017-0219.1).
- Rezaie, M., A. Moradzadeh, and A. Nejati Kalate, 2017a, 3D gravity data-space inversion with sparseness and bound constraints: *Journal of Mining and Environment*, **8**, 227–235, doi: [10.22044/jme.2015.558](https://doi.org/10.22044/jme.2015.558).
- Rezaie, M., A. Moradzadeh, and A. Nejati Kalate, 2017b, Fast 3D inversion of gravity data using solution space prior conditioned Lanczos bidiagonalization: *Journal of Applied Geophysics*, **136**, 42–50, doi: [10.1016/j.jappgeo.2016.10.019](https://doi.org/10.1016/j.jappgeo.2016.10.019).
- Rezaie, M., A. Moradzadeh, A. Nejati Kalate, and H. Aghajani, 2016, Fast 3D focusing inversion of gravity data using reweighted regularized Lanczos bidiagonalization method: *Pure and Applied Geophysics*, **174**, 359–374, doi: [10.1007/s00024-016-1395-8](https://doi.org/10.1007/s00024-016-1395-8).
- Santos, D. F., J. B. C. Silva, C. M. Martins, R. D. C. S. dos Santos, L. C. Ramos, and A. C. M. de Araújo, 2015, Efficient gravity inversion of discontinuous basement relief: *Geophysics*, **80**, no. 4, G95–G106, doi: [10.1190/geo2014-0513.1](https://doi.org/10.1190/geo2014-0513.1).
- Tikhonov, A. N., and V. Y. Arsenin, 1977, Solutions of ill-posed problems: *Mathematics of Computation*, **32**, 491–491.
- Vatankhah, S., V. E. Ardestani, and R. A. Renaut, 2014, Automatic estimation of the regularization parameter in 2D focusing gravity inversion: Application of the method to the Safo manganese mine in the northwest of Iran: *Journal of Geophysics and Engineering*, **11**, 45001, doi: [10.1088/1742-2132/11/4/045001](https://doi.org/10.1088/1742-2132/11/4/045001).
- Wang, T., D. Huang, G. Ma, Z. Meng, and Y. Li, 2017, Improved preconditioned conjugate gradient algorithm and application in 3D inversion of gravity-gradiometry data: *Applied Geophysics*, **14**, no. 2, 301–313, doi: [10.1007/s11770-017-0625-x](https://doi.org/10.1007/s11770-017-0625-x).
- Xu, Z., L. Wan, and M. S. Zhdanov, 2020, Focusing iterative migration of gravity gradiometry data acquired in the Nordkapp Basin, Barents Sea: *Geophysical Prospecting*, **68**, 2292–2306, doi: [10.1111/1365-2478.12990](https://doi.org/10.1111/1365-2478.12990).
- Yao, C., T. Hao, Z. Guan, and Y. Zhang, 2003, High-speed computation and efficient storage in 3-D gravity and magnetic inversion based on genetic algorithms: *Chinese Journal of Geophysics*, **2**, 252–258.
- Zhang, J., and L. Jiang, 2017, Analytical expressions for the gravitational vector field of a 3-D rectangular prism with density varying as an arbitrary-order polynomial function: *Geophysical Journal International*, **210**, 1176–1190, doi: [10.1093/gji/ggx230](https://doi.org/10.1093/gji/ggx230).
- Zhang, N., Y. Wu, S. Zhou, and P. Sun, 2019, 3D inversion of airborne gravity gradient data for physical properties based on optimizing constraints of spatial position of the geologic body: *Chinese Journal of Geophysics*, **62**, 1515–1525.
- Zhdanov, M. S., and E. Tartaras, 2002, Three-dimensional inversion of multitransmitter electromagnetic data based on the localized quasi-linear approximation: *Geophysical Journal International*, **148**, 506–519, doi: [10.1046/j.1365-246X.2002.01591.x](https://doi.org/10.1046/j.1365-246X.2002.01591.x).
- Zhou, X., 2009, 3D vector gravity potential and line integrals for the gravity anomaly of a rectangular prism with 3D variable density contrast: *Geophysics*, **74**, no. 6, I43–I53, doi: [10.1190/1.3239518](https://doi.org/10.1190/1.3239518).

Biographies and photographs of the authors are not available.